

Modeling of nonlinear microscopy of localized field enhancements in random metal nanostructures

Jonas Beermann* and Sergey I. Bozhevolnyi

Department of Physics and Nanotechnology, Aalborg University, Skjernvej 4A, DK-9220 Aalborg, Denmark

Victor Coello

CICESE Monterrey, Ángel Martínez Villarreal 425, Col. Chepevera, Monterrey Nuevo León, C.P. 64030 S.N. de los Garza N.L., Mexico

(Received 10 November 2005; revised manuscript received 12 January 2006; published 13 March 2006)

Nonlinear microscopy of localized field enhancements in random metal nanostructures with a tightly focused laser beam scanning over a sample surface is modeled by making use of analytic representations of the Green dyadic in the near- and far-field regions, with the latter being approximated by the part describing the scattering via excitation of surface plasmon polaritons. The developed approach is applied to scanning second-harmonic (SH) microscopy of small gold spheres placed randomly on a gold surface. We calculate self-consistent fundamental harmonic (FH) and SH field distributions at the illuminated sample surface and, thereby, FH and SH images for different polarization configurations of the illuminating and detected fields. The simulated images bear close resemblance to the images obtained experimentally, exhibiting similar sensitivity to the wavelength and polarization, as well as sensitivity to the scattering configuration. We verify directly our conjecture that very bright spots in the SH images occur due to the spatial overlap of properly polarized FH and SH eigenmodes. Applications and further improvements of the developed model are discussed.

DOI: [10.1103/PhysRevB.73.115408](https://doi.org/10.1103/PhysRevB.73.115408)

PACS number(s): 78.67.-n, 42.65.Ky, 73.20.Mf, 02.60.-x

I. INTRODUCTION

Light-matter interactions in nanostructured materials give rise to nanostructured optical fields whose distinctive properties bring about various fascinating phenomena, including light localization, photonic band gap effects, and surface enhanced scattering.^{1,2} A profound understanding of fundamental and applied aspects of these phenomena becomes increasingly vital for further progress in nanoscience and nanotechnology. One of the most remarkable effects in light scattering by *metal* nanostructures is the strong (up to several orders of magnitude) and spatially localized (on nanometer scale) field intensity enhancement. This enhancement can occur due to the resonance excitation of localized surface plasmons (SPs) associated with individual (noninteracting, e.g., rarely spaced) scatterers.³ In the system of strongly interacting random nanoparticles, resonant SP excitations (eigenmodes of the system) are due to multiple interparticle light scattering and are associated rather with a global than local arrangement of scatterers. These eigenmodes tend to be localized in nm-sized volumes with resonance frequencies covering a wide spectrum range from near UV to far IR and exhibit very different strength, phase, polarization, and localization characteristics.^{4,5} If scatterers are placed in the vicinity of a metal surface that supports the propagation of surface plasmon polaritons (SPPs), the interparticle electromagnetic interaction can be facilitated and further enhanced due to the SPPs that provide an additional interaction channel.⁶ Resonant (system) eigenmodes were the subject of many experiments concerned with near-field imaging of disordered metal nanostructures.⁷⁻¹² It is, however, important to note that these experiments dealt with *linear* scattering, i.e., localized intensity enhancement has been observed at the frequency of the illumination.

The strong local field intensity enhancement in light scattering by metal nanostructures plays a major role in Raman

scattering and in the second-harmonic (SH) generation (SHG). Enhanced SH generation at rough metal surfaces has been the subject of numerous experimental and theoretical investigations concerned mainly with the angular distribution of far-field SH radiation.¹³ Spatially resolved SH measurements at rough metal surfaces conducted with a near-field microscope have also been reported^{14,15} with the observed local SH enhancement being ascribed to the SP localization¹⁴ or the lightning rod effect.¹⁵ However, bright regions seen in the SH images obtained in the first case were rather diffuse and noisy, and the suggested origin (localization) was not corroborated with, e.g., wavelength dependent measurements. Recently, strongly enhanced SH generations characterized by a broad angular (far-field) distribution have been observed with gold-glass films near the percolation threshold.¹⁶ A large diffuse SH component indicates (though *indirectly*) the occurrence of localized SPs that generate strongly fluctuating (in amplitude, phase, and polarization) local SH sources. In addition, direct observations (using far-field SH microscopy) of localized SH enhancements were later reported with similar films.¹⁷ For both these samples the random gold particles formed only semicontinuous films on insulating silica substrates. At the same time, we used SH far-field scanning optical microscopy (SOM) to image randomly distributed gold scatterers deposited on a gold film supporting a multiple scattering of SPPs.^{18,19} We observed strongly enhanced localized SH spots, exhibiting sensitivity to the wavelength and polarization, as well as sensitivity to the scattering configuration.

Comparing SOM images obtained at fundamental harmonic (FH) and SH frequencies, we inferred that SHG occurs most efficiently at sites where the FH and SH eigenmodes spatially overlap. This conjecture has been qualitatively supported by the results of numerical simulations (within the quasistatic approximation) of SHG in a metallic nanosystem, a random planar composite, whose entire

extent is much smaller than the light wavelength.²⁰ These results are, however, of limited use when interpreting SH-SOM images obtained with a tightly focused laser beam scanning over a nanostructured metal surface. It seems plausible to expect that *local* illumination and SHG would *selectively* excite FH and SH eigenmodes whose interaction can be mediated by SPPs, resulting in an intricate interplay of the FH and SH field distributions for global and local excitations and the corresponding SOM images.

Theoretical modeling of the SH-SOM of nanostructures is quite a challenge in itself, because one has to deal with two coupled problems of multiple light scattering, i.e., one has to find self-consistent fields at both FH and SH frequencies.²¹ A microscopic self-consistent approach to this problem developed by making use of the generalized Green dyadic is quite complicated and can be applied only to a very limited number of scatterers.²¹ In this paper, we consider SH-SOM of nanostructures, i.e., small metal spheres placed on a metal substrate, within the framework of a point-dipole approximation with the Green dyadic being approximated by analytic expressions available for the near- and far-field regions. While the near-field approximation of the Green dyadic is well-known (see, e.g., Ref. 22), the far-field analytic expression is based on the recently established fact that, near a metal surface and for sufficiently large distances from a scattering source, the Green dyadic can be approximated by its part associated with the SPP excitation.²³ Our modeling involves several intervening stages. First, the self-consistent FH field established in a scattering system is determined in relation to a position of a tightly focused scanning FH beam illuminating the sample. Secondly, the self-consistent SH field (driven by the self-consistent FH field) is found in the scattering system. Finally, thus determined (for each position of the incident beam) FH and SH fields are used to calculate the corresponding field intensities at the site of a remote detector, resulting in FH and SH images. The results of numerical simulations are presented for gold (identical) nanoparticles randomly placed on a gold substrate and compared with the experimental results reported previously.^{18,19}

II. THE SELF-CONSISTENT FIELD

The problem of multiple scattering in a system of nanoparticles, which are placed near a metal surface and illuminated by an incident electric field $\mathbf{E}^0(\mathbf{r})$ at the wavelength λ , can be treated in the electric-dipole approximation, i.e., by treating each nanoparticle as a dipolar scatterer.²² A detailed consideration of the point-dipole approximation for SPP scattering, and its limitations imposed by the energy conservation, can be found in Ref. 24. In this approximation and considering identical particles, the self-consistent electric fields established at the sites of nanoparticles in the process of multiple scattering can be found by solving the following equation:

$$\mathbf{E}(\mathbf{r}_i) = \mathbf{E}^0(\mathbf{r}_i) + k_0^2 \sum_{j \neq i}^N \mathbf{G}(\mathbf{r}_i, \mathbf{r}_j) \cdot \boldsymbol{\alpha} \cdot \mathbf{E}(\mathbf{r}_j), \quad (1)$$

where $\mathbf{E}(\mathbf{r}_i)$ is the self-consistent electric field at the site \mathbf{r}_i of particle i , $\boldsymbol{\alpha}$ is the polarizability tensor of a particle with

surface dressing, i.e., multiple scattering between the particle and the metal surface taken into count, $k_0 = 2\pi/\lambda$ is the free-space wave number, $\mathbf{E}^0(\mathbf{r}_i)$ is the incident electric field at the site of particle i , and $\mathbf{G}(\mathbf{r}_i, \mathbf{r}_j)$ is the total Green dyadic describing the field propagation from a source point \mathbf{r}_j to an observation point \mathbf{r}_i . This total Green dyadic is composed of a direct (free-space) dyadic \mathbf{G}^d and the indirect dyadic \mathbf{G}^s describing both the reflection from the metal surface and the excitation of SPPs.²²

The polarizability of a spherical nanoparticle in free space can be approximated in the electrostatic limit (when the particle is much smaller than the light wavelength) as follows:

$$\boldsymbol{\alpha}^0 = \varepsilon_0 U 4\pi a^3 \frac{\varepsilon - 1}{\varepsilon + 2}, \quad (2)$$

where ε is the dielectric (wavelength dependent) function of the particle, a is its radius, ε_0 is the vacuum permittivity, and U is the unit tensor. However, due to the multiple scattering between the particle and the surface, the so-called surface dressing, the polarizability used in Eq. (1) for particles located near the surface, is different from that in free space and given by

$$\boldsymbol{\alpha} = \left(\mathbf{U} - k_0^2 \frac{\boldsymbol{\alpha}^0}{\varepsilon_0} \cdot \mathbf{G}^s(\mathbf{r}, \mathbf{r}) \right)^{-1} \cdot \boldsymbol{\alpha}^0, \quad (3)$$

where \mathbf{r} is the center of the particle. In the image dipole (electrostatic) approximation for the indirect contribution \mathbf{G}^s (Refs. 22, 25, and 26) to the total Green dyadic and for a spherical particle placed in contact with the surface, the surface dressed polarizability reads²³

$$\boldsymbol{\alpha} \approx \left[\mathbf{U} - \frac{\varepsilon - 1}{\varepsilon + 1} \frac{\varepsilon - 1}{\varepsilon + 2} \left(\frac{1}{8} \hat{x}\hat{x} + \frac{1}{8} \hat{y}\hat{y} + \frac{1}{4} \hat{z}\hat{z} \right) \right]^{-1} \cdot \boldsymbol{\alpha}^0, \quad (4)$$

where \hat{x} , \hat{y} , \hat{z} are the coordinate unit vectors in the coordinate system with the vector \hat{z} being perpendicular to the air-gold interface and the dielectric constant of the substrate set equal to that of the particle.

Using Eq. (4) for the polarizability of the nanoparticles together with the appropriate Green dyadic \mathbf{G} , one can determine the self-consistent fields at the sites of all particles from Eq. (1) and then find the total electric field everywhere outside the particles using the following expression:

$$\mathbf{E}(\mathbf{r}) = \mathbf{E}^0(\mathbf{r}) + k_0^2 \sum_i^N \mathbf{G}(\mathbf{r}, \mathbf{r}_i) \cdot \boldsymbol{\alpha} \cdot \mathbf{E}(\mathbf{r}_i). \quad (5)$$

However, in order to accomplish this task, it still remains to identify such an appropriate Green dyadic.

III. THE GREEN DYADIC

Considering both the source and observation points being close to a metal surface but far away from each other, one can approximate the total Green dyadic (which includes the direct and indirect terms) with the part of the indirect Green dyadic concerned with the excitation of SPPs.²³ In this approximation, which is actually asymptotically correct as the in-plane separation of source and observation points in-

creases towards infinity,²⁷ the Green dyadic can be represented by

$$\mathbf{G}_{\text{spp}}(\mathbf{r}, \mathbf{r}') \approx a_{zz}(\lambda) \exp[i\kappa_z(z+h)] H_0^1(\kappa_\rho \rho) \times \left[\hat{z}\hat{z} + (\hat{z}\hat{\rho} - \hat{\rho}\hat{z}) \frac{\kappa_z}{\kappa_\rho} - \hat{\rho}\hat{\rho} \left(\frac{\kappa_z}{\kappa_\rho} \right)^2 \right], \quad (6)$$

where H_0^1 is the zero-order Hankel function of the first kind, $\rho = |\mathbf{r}_\parallel - \mathbf{r}'_\parallel|$, $\hat{\rho} = (\mathbf{r}_\parallel - \mathbf{r}'_\parallel)/\rho$, with \parallel referring to the projection of the radius vector on the xy plane, which coincides with the metal-air interface, and z refers to the height of the observation point \mathbf{r} above the surface, while h refers to the height of the source point \mathbf{r}' . Finally, κ_ρ and κ_z are the components of the three-dimensional SPP wave vector

$$\kappa_\rho = k_0 \sqrt{\frac{\varepsilon}{\varepsilon + 1}}, \quad (7)$$

$$\kappa_z = \sqrt{k_0^2 - \kappa_\rho^2}, \quad (8)$$

and

$$a_{zz}(\lambda) = \frac{\kappa_\rho}{2} \left[\sqrt{\varepsilon} \left(1 - \frac{1}{\varepsilon^2} \right) \frac{1 + \varepsilon}{\varepsilon} \right]^{-1}, \quad (9)$$

where it is understood that the dielectric constant ε of metal depends on the wavelength. In calculations, for the dielectric constant ε of gold, we used bulk values obtained from a linear interpolation of the data listed in Ref. 28.

The above Green dyadic approximation has been shown to noticeably deviate from the exact total Green dyadic for small distances (less than a few wavelengths) between the source and observation points.²³ On the other hand, its usage for simulations of the SPP band gap structures consisting of nanoparticles arranged in a periodic pattern gave quite reasonable results even though the interparticle distance was close to half of the light wavelength.²³ However, for randomly placed nanoparticles with relatively high densities,^{18,19} some particles are in or close to contact with each other so that the interparticle distances can be down to a small fraction of the wavelength, i.e., in the near-field domain. In such a case, one can take advantage of the near-field (electrostatic) approximation of the total Green dyadic that can also be expressed in a simple analytic form:²²

$$\mathbf{G}_{\text{nf}}(\mathbf{r}, \mathbf{r}', \omega) = \mathbf{D}_{\text{nf}}(\mathbf{r}, \mathbf{r}', \omega) + \mathbf{I}_{\text{nf}}(\mathbf{r}, \mathbf{r}', \omega), \quad (10)$$

where $\mathbf{D}_{\text{nf}}(\mathbf{r}, \mathbf{r}', \omega)$ is the direct part of the near-field propagator given by

$$\mathbf{D}_{\text{nf}}(\mathbf{r}, \mathbf{r}', \omega) = -\frac{c^2}{4\pi\omega^2} \frac{3\mathbf{e}_R \mathbf{e}_R - \mathbf{U}}{R^3} \quad (11)$$

with $R = |\mathbf{r} - \mathbf{r}'|$, $\mathbf{e}_R = (\mathbf{r} - \mathbf{r}')/R$, and \mathbf{U} being the unit tensor, while the indirect part $\mathbf{I}_{\text{nf}}(\mathbf{r}, \mathbf{r}', \omega)$ of the near-field propagator, for the air-metal interface coinciding with the plane $z = 0$, can be expressed as

$$\mathbf{I}_{\text{nf}}(\mathbf{r}, \mathbf{r}', \omega) = \mathbf{D}_{\text{nf}}(\mathbf{r}, \mathbf{r}_{ms}, \omega) \cdot \mathbf{M}(\omega), \quad (12)$$

with $\mathbf{r}_{ms} = (x', y', -z')$ pointing to the position of the mirror image of the source point and

$$\mathbf{M}(\omega) = \frac{\varepsilon - 1}{\varepsilon + 1} \begin{pmatrix} -1 & 0 & 0 \\ 0 & -1 & 0 \\ 0 & 0 & 1 \end{pmatrix}. \quad (13)$$

Transition between \mathbf{G}_{nf} and \mathbf{G}_{spp}

Both approximations considered above are limited to either short or long interaction distances. The main idea of our approach is to use the near-field dyadic [Eq. (10)] for distances shorter, and the SPP dyadic [Eq. (6)] for distances longer, than a certain (transition) distance related to a specified fraction of the light wavelength used in the particular simulations. A natural requirement to such a transition distance would then be that no apparent (unphysical) jumps should be seen in the dyadic components when switching from one expression to another one.

In order to find a proper distance for the transition between the two dyadics, the radial dependence of the nonzero dyadic components G_{zz} , G_{xx} and $G_{zx} = G_{xz}$ were calculated using accordingly Eqs. (6) and (10) at different distances from the (gold) surface and for different transition distances at the wavelength of 750 nm. Based on these calculations the transition distance of $3\lambda/5$ was chosen (Fig. 1). It should be noted here that the near-field parts of components G_{zz} , G_{xx} are both one order of magnitude larger than the remaining nonzero component $G_{zx} = G_{xz}$. Furthermore, the real parts of these components are approximately one order of magnitude larger than their imaginary parts. However, generally speaking, it is not possible to find the transition distance that would ensure smooth transitions for all dyadic components. For example, the transition of the G_{zx} component seems rather abrupt (Fig. 1). Nevertheless, one should bear in mind that the aim is to develop a relatively simple approach using analytic *approximations* of the total Green dyadic, so as to be able of dealing with a complex surface system with many strongly interacting particles. So, the Green dyadic used throughout the presented simulations is set to the following form:

$$\mathbf{G}(\mathbf{r}, \mathbf{r}') = \begin{cases} \mathbf{G}_{\text{nf}}(\mathbf{r}, \mathbf{r}') & \text{for } |\mathbf{r} - \mathbf{r}'| \leq 3\lambda/5, \\ \mathbf{G}_{\text{spp}}(\mathbf{r}, \mathbf{r}') & \text{for } |\mathbf{r} - \mathbf{r}'| > 3\lambda/5. \end{cases} \quad (14)$$

It should be understood that the proper transition distance cannot be determined exactly. The influence of this will be discussed later in this paper.

IV. SIMULATION CONFIGURATION

The simulation configuration with multiple scattering between spherical gold particles, positioned on a smooth gold surface, and scattering into far-field radiation reaching remote detectors is schematically shown in Fig. 2. Based on the composed Green dyadic [Eq. (14)] it is now possible to solve Eq. (1) and use Eq. (5) to find the self-consistent field distribution $\mathbf{E}(\mathbf{r})$ for a given incident electric field $\mathbf{E}^0(\mathbf{r})$ and a set of particles located at \mathbf{r}_i . Here it is important to note that the interaction of the dipole with itself is already taken care of in the polarizability in Eq. (4) and the case $i=j$, giving $R=0$, is therefore omitted in Eq. (1). It transpires that the

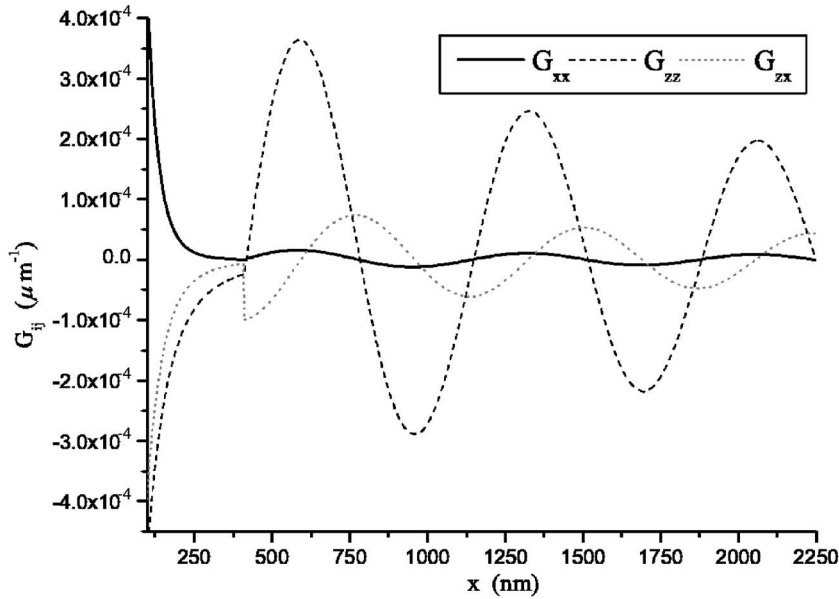


FIG. 1. Nonzero dyadic components calculated at the height of 40 nm above the gold surface for $\lambda=750$ nm using the near-field and SPP dyadic for distances correspondingly smaller and larger than the transition distance of $3\lambda/5$.

next steps towards the simulations should be the description of particle sets and an incident field scanning over the surface.

A. Sample description

In order to simulate samples with random surface nanostructures, we generated different sets of random x and y coordinates of the centers of spherical particles having the same radius a and being placed directly on the surface plane ($z=0$). When generating these sets, one should control the smallest allowed separation between the particles to avoid an already occupied scatter region to be taken by another or more scatterers. One can, for example, employ an algorithm preventing the distance between particle centers from being less than $2a$, leading at the most to touching spheres. In the dipole approximation, however, such an approach of geometrically touching spheres has been shown to fail describing long-wavelength resonances observed in groups of particles, where proximity effects should be taken into account.²⁹ One solution to this problem can be the implementation of interacting high-order multipole moments into the calculation, but this will result in essentially intractable problems for large groups of particles.³⁰ Meanwhile it is possible to obtain a description of the optical response of an arbitrary shaped object and still remain within the dipole approximation.^{30–32} The general idea in such a description is that originally touching spheres should be replaced by overlapping spheres with the dipole moments located at their centers, since this would avoid underestimating the interaction between the spheres. One suggestion for this corrected minimum separation d_{min} can be found from the following relation:³²

$$d_{min}^3 = (4\pi/3)a^3, \quad (15)$$

which gives

$$d_{min} = 1.612a = 0.806(2a). \quad (16)$$

We have adopted the above procedure and generated two samples covered by $5 \times 5 \mu\text{m}^2$ areas of the high and low density of spherical scatterers: 50 and 10 per μm^2 , respectively. The scatterers placed on $7 \times 7 \mu\text{m}^2$ smooth gold areas are chosen to have radii $a=40$ nm, and their positions are depicted in Fig. 3 as circles with approximately true dimensions.

B. Incident field

The incident electric field is considered to be formed by an incident (normal to the air-gold interface) Gaussian-

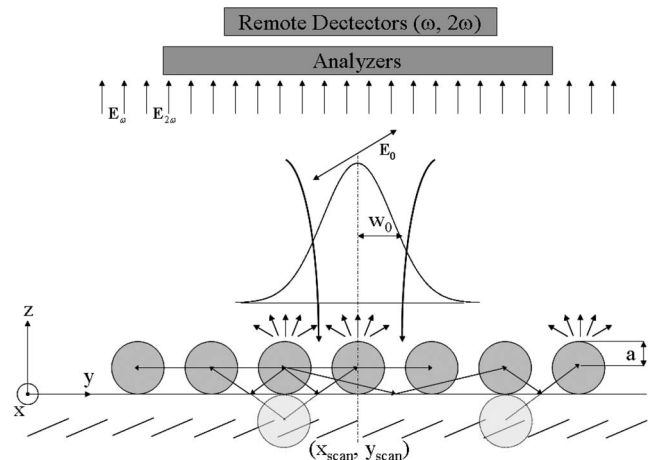


FIG. 2. Schematic of the simulation configuration. A Gaussian-shaped (scanning) beam with center coordinates (x_{scan}, y_{scan}) is incident normal to the air-gold interface with randomly positioned spherical gold particles resulting in strong multiple scattering and SHG. The polarization of the incident FH as well as the FH and SH radiation is controlled by selecting the corresponding components of the reflected electric fields.

shaped beam with linear polarization and its reflection by the interface

$$E^0(\mathbf{r}) = \mathbf{e}_p E^0 \exp\left(-\frac{(x-x_{\text{scan}})^2 + (y-y_{\text{scan}})^2}{w_0^2}\right) \times (e^{ik_0z} + \gamma e^{-ik_0z}), \quad (17)$$

where E^0 is the field amplitude, the polarization along either \hat{x} or \hat{y} is defined by the vector $\mathbf{e}_p = (1, 0, 0)$ or $\mathbf{e}_p = (0, 1, 0)$, respectively, the beam center is located at the scanning coordinates $(x_{\text{scan}}, y_{\text{scan}})$, and w_0 is the beam radius at the intensity level of e^{-1} . Finally, the phase difference between the incident and the reflected fields at a height z above the surface is incorporated by the last term, where $\gamma = (1-n)/(1+n)$ is the reflection coefficient of the gold surface having refractive index $n = \sqrt{\epsilon}$.

C. FH- and SH-SOM image formation

Starting with the incident field as in Eq. (17) and using this field $E^0(\mathbf{r}_i)$ at the centers of all scatterers, one can proceed to solving Eq. (1) with the proper Green dyadic $\mathbf{G}(\mathbf{r}_i, \mathbf{r}_j)$ from Eq. (14) and determining the self-consistent fields $\mathbf{E}(\mathbf{r}_i)$ at the positions of all scatters. The FH-SOM image can then be calculated by summing up the scattered fields from all scatterers and the reflected (by a flat metal surface) incident field at the position of a remote detector. The first contribution is proportional to the sum of the corresponding in-plane fields at the sites of scatterers²¹ weighted with the factor depending on an effective aperture of the detector so as to correctly balance the signals from the reflected Gaussian beam and the scattered fields. We have chosen to use an effective factor whose value is selected from the appearance of the experimental and simulated images (for the parallel polarization configurations). For example, the intensity in FH-SOM images, for both incident and detected polarizations being parallel to the x axis, were simulated as follows:

$$I_{\omega}^{\text{xx}}(x_{\text{scan}}, y_{\text{scan}}) = \left| \Gamma E^{\text{refl}} + \sum_i^N E_x(\omega, \mathbf{r}_i) \right|^2, \quad (18)$$

where

$$E^{\text{refl}} = \gamma e^{-ik_0a} = \frac{1-n}{1+n} e^{-ik_0a} \quad (19)$$

contain the reflection coefficient and phase used in the last term of Eq. (17). In our case $\Gamma = 100$ was selected in order to obtain qualitative agreement in the image contrast with experimental FH images of random gold nanostructures.^{18,19} For the cross-polarized configurations, the reflected incident field is not detected and $\Gamma = 0$ was used.

Simulation of the SH-SOM images is more complicated and requires several calculation steps. The main circumstance to be kept in mind is that, for symmetry reasons, metals do not possess second-order susceptibilities $\chi^{(2)}$ in bulk.³³ SH fields can therefore be generated only at the (flat) metal surface and at the scatterers (though the latter process, occurring insofar as *spherical* particles are being close to the metal surface, is not efficient). In any case, the contribution to SHG

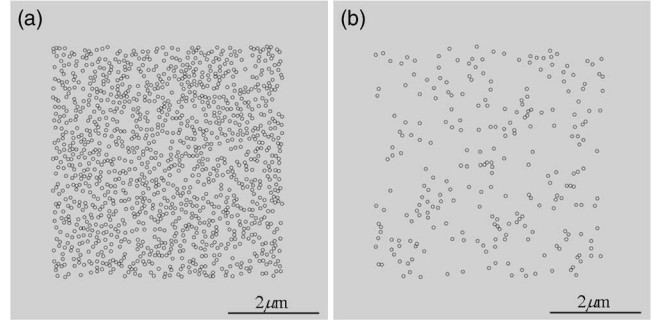


FIG. 3. Gray-scale representations ($7 \times 7 \mu\text{m}^2$) of the generated samples with centered $5 \times 5 \mu\text{m}^2$ areas with (a) the high density ($50 \mu\text{m}^{-2}$) and (b) low density ($10 \mu\text{m}^{-2}$) of spherical scatterers with 40-nm radius.

from the z component (normal to the surface) of the FH field would significantly exceed those from the x and y components (parallel to the surface). To simplify the consideration, we assumed that the main source of SH radiation are the z components of the SH field at the sites of scatterers $E_z^0(2\omega, \mathbf{r}_i)$, which are proportional to the SH z components at the surface driven by the FH z component at the surface $E_z(\omega, x_i, y_i, z=0)$, and that the latter is proportional to the FH z component at the sites of scatterers:

$$E_z^0(2\omega, \mathbf{r}_i) \propto E_z(2\omega, x_i, y_i, z=0) \propto E_z^2(\omega, x_i, y_i, z=0) \propto E_z^2(\omega, \mathbf{r}_i). \quad (20)$$

This SH field distribution (at the sites of scatterers) was then used as an incident SH field $E_z^0(2\omega, \mathbf{r}_i)$ in order to determine the self-consistent SH field $\mathbf{E}(2\omega, \mathbf{r}_i)$ by solving (as in the FH case) the self-consistent equation for SH fields analogous to Eq. (1). The SH-SOM images were simulated similarly to the FH-SOM images by summing up the in-plane components of SH fields. For example, in the case of different polarizations of the incident FH (x polarization) and detected SH (y polarization) fields, the SH image was calculated as follows:

$$I_{2\omega}^{\text{xy}}(x_{\text{scan}}, y_{\text{scan}}) = \left| \sum_i^N E_y(2\omega, \mathbf{r}_i) \right|^2. \quad (21)$$

V. NUMERICAL RESULTS

The approach adopted in this work does not allow direct examination of the field eigenmodes as, for example, was performed in Ref. 20. Instead, one can investigate the self-consistent field distributions (for different illumination conditions) whose bright spots (field enhancements) indicate implicitly the existence of eigenmodes. Since the field distributions in the case of strong multiple scattering depend upon the illumination configuration,¹ we start our modeling of the two scattering systems (Fig. 3) by considering the case of a plane-wave illumination at the FH frequency. The formation of FH and SH images obtained with the SOM will then be considered followed by a discussion of their features and a comparison with the experimental results.^{18,19}

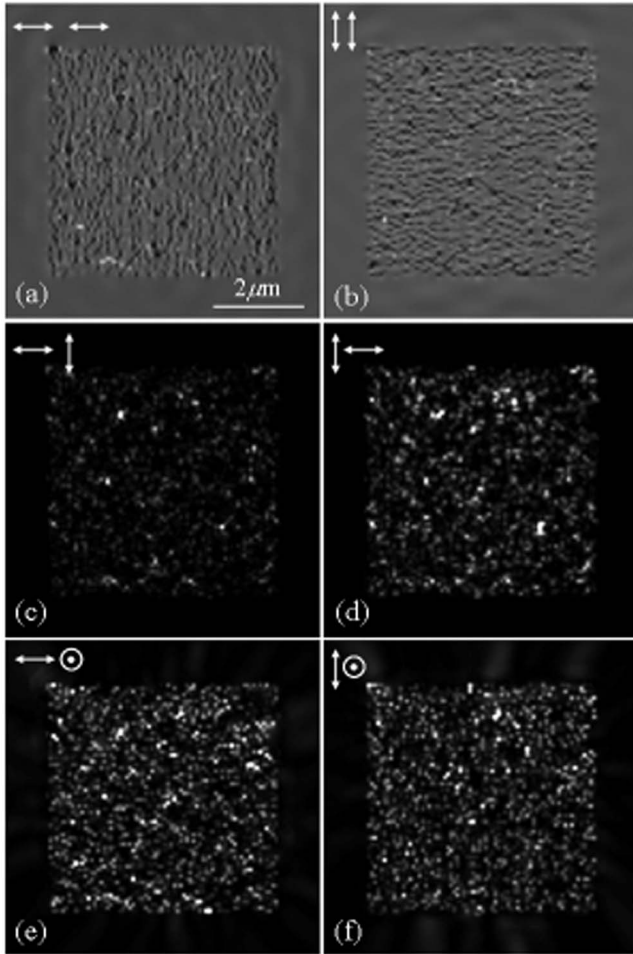


FIG. 4. Gray-scale images ($7 \times 7 \mu\text{m}^2$) of the distributions of squared magnitudes of the field components for the high-density sample obtained with the wavelength of 750 nm at the polarization configurations indicated by arrows (excitation, left arrow; detection, right arrow). The maximum levels (in relative units) are at (a) 10.3, (c) 4.4, and (e) 6.8—all with x -polarized excitation, and (b) 9.4, (d) 2.1, and (f) 7.2—all with y -polarized excitation.

A. FH field distributions

In order to examine and compare scattering processes occurring in the considered configurations, we calculated the FH field distribution $\mathbf{E}(x, y, z=2a+10 \text{ nm})$ at a fixed height of 10 nm above the particles illuminated by a plane wave at normal incidence for different wavelengths and polarizations. In this simulation configuration, the incident beam radius in Eq. (17) is set to $w_0 \rightarrow \infty$ with the beam center being kept at the coordinate origin, i.e. $(x_{\text{scan}}, y_{\text{scan}}) = (0, 0)$. For two perpendicular polarizations of the incident plane wave with the wavelength of 750 nm, the squared magnitudes of the self-consistent field components, $|E_x|^2$, $|E_y|^2$, and $|E_z|^2$, are shown in Figs. 4 and 5 for the high- and low-density samples, respectively.

Close inspection of the positions of bright spots for the high-density sample (Fig. 4) reveals that, apart from bright spots coinciding in location with individual scatterers, quite a few bright spots are actually situated next to and between the

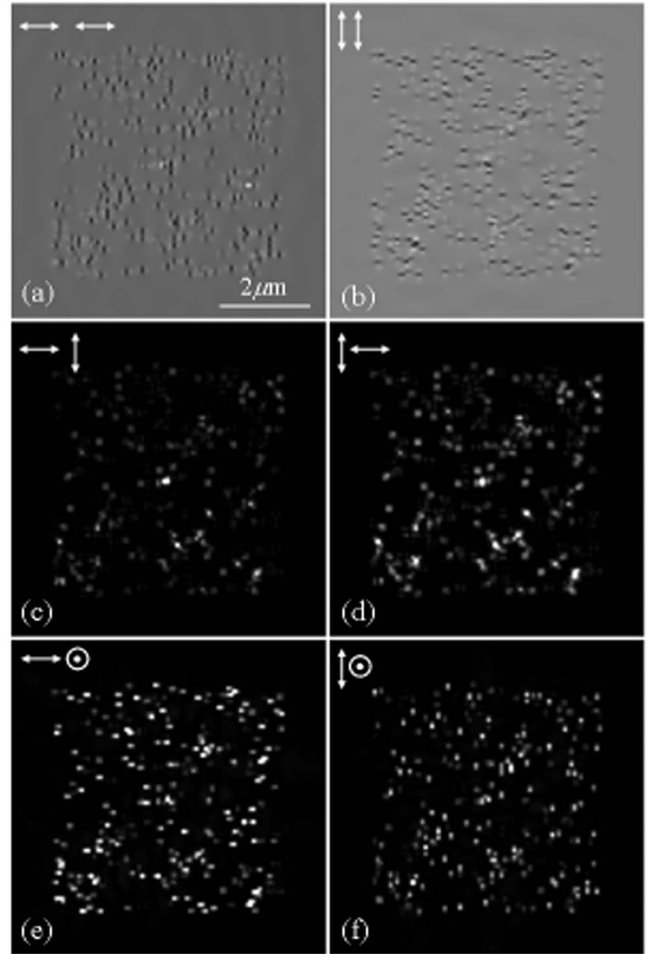


FIG. 5. Gray-scale images ($7 \times 7 \mu\text{m}^2$) of the distributions of squared magnitudes of the field components for the low-density sample obtained with the wavelength of 750 nm at the polarization configurations indicated by arrows (excitation, left arrow; detection, right arrow). The maximum levels (in relative units) are at (a) 6.9, (c) 1.18, and (e) 2—all with x -polarized excitation, and (b) 5.7, (d) 0.66, and (f) 3—all with y -polarized excitation.

scatterers, a feature that indicates the occurrence of strong multiple scattering in the system.¹ In addition, the positions of bright spots are seen to be different for different polarization configurations, with the intensity levels for parallel and cross-polarized configurations being of the same order of magnitude. It should be kept in mind that strong depolarization is inherently related to strong multiple scattering. Furthermore, the field component perpendicular to the sample surface is seen to reach similar magnitudes [Figs. 4(e) and 4(f)], suggesting that the process of multiple scattering is mediated via SPP excitation and scattering. At any rate, a dipolar scatterer placed close to a metal surface and driven with an electric field perpendicular to the surface scatters a significant part of radiation in the form of SPPs.²⁷ It is also seen that the images corresponding to the copolarized configurations [Figs. 4(a) and 4(b)] exhibit faint quasiperiodic fringes oriented perpendicular to the polarization direction. These fringes are the result of interference between the incident and scattered fields, indicating thereby that the latter

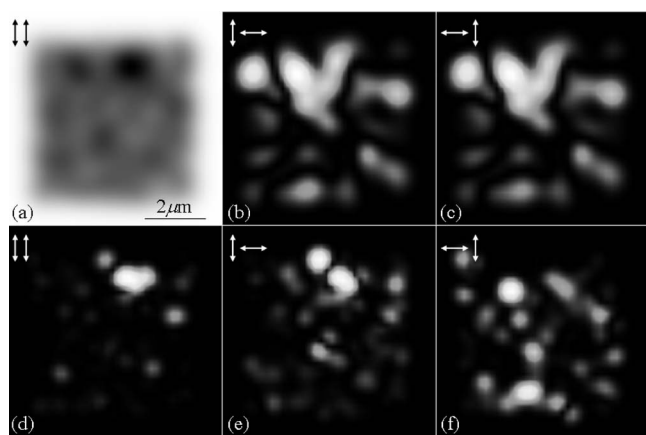


FIG. 6. Gray-scale (a)–(c) FH and (d)–(f) SH images ($7 \times 7 \mu\text{m}^2$) of the high-density sample simulated for the wavelength of 750 nm and the polarization configurations indicated by arrows (excitation, left arrow; detection, right arrow). The maximum signals are 9700, 13, and 13 for FH and 0.075, 0.055, and 0.035 for SH images.

contain indeed SPPs (that propagate in the direction of the in-plane polarization). Finally, the field distributions simulated at other wavelengths, e.g., at the wavelengths of 700 and 800 nm, were found to be similar to those at 750 nm but having different relative intensities of the bright spots, which is again one of the features inherent for multiple scattering.^{1,2,4,5} The corresponding images calculated with the low-density sample (Fig. 5) bear close resemblance to those obtained for the high-density sample (Fig. 4). All aforementioned features related to multiple scattering and the influence of SPP excitation can be seen on these images albeit somewhat less pronounced. Thus, intensity levels for the cross-polarized configurations are considerably smaller than those for the parallel polarizations, indicating that the process of multiple scattering is not so strong for the low-density sample as compared to that which occurred for the high-density sample. The field component perpendicular to the sample surface is also significantly smaller [Figs. 5(e) and 5(f)] and quasiperiodic fringes—less pronounced [Figs. 5(a) and 5(b)] in this case, indicating that the SPP excitation and scattering occur less efficiently. Note that such a difference in scattering for the high- and low-density samples could, in principle, be inferred from theoretical studies^{4,5} and experimental investigations.¹⁹ However, the images obtained provide also quantitative information on the strength of depolarization and SPP influence in the considered scattering systems.

B. FH- and SH-SOM images

The FH- and SH-SOM images were calculated with the incident field chosen as in Eq. (17) with the beam radius set to $w_0=0.5 \mu\text{m}$ and taken at the centers of the particles ($z=a$). Using the procedure described in Sec. IV C, we calculated the FH and SH images of the high-density sample for various polarization configurations at the incident light wavelength of 750 and 800 nm (Figs. 6 and 7, respectively).

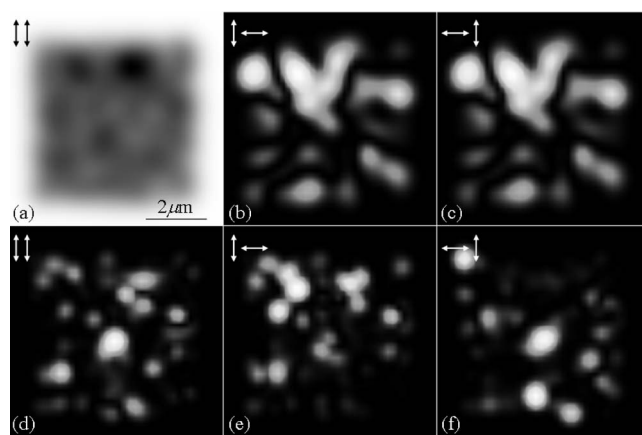


FIG. 7. Gray-scale (a)–(c) FH and (d)–(f) SH images ($7 \times 7 \mu\text{m}^2$) of the high-density sample simulated for the wavelength of 800 nm and the polarization configurations indicated by arrows (excitation, left arrow; detection, right arrow). The maximum signals are 9700, 8, and 8 for FH and 0.014, 0.012, and 0.022 for SH images.

The transition distance used to obtain all images presented in this paper was 0.6λ as described by Eq. (14). However, we have investigated the sensitivity of FH and SH images to this value and within the interval $(0.4-0.8)\lambda$ we observed that the FH images remained almost identical, while the SH images showed a change in the mutual relative strength of the SH bright spots and with the SH images showing the largest changes for shorter transition distances.

It is seen that the appearance of both FH and SH images is similar to that of experimentally obtained images with the main feature of the occurrence of SH bright spots, whose locations depend on the light wavelength and polarization, being clearly reproduced.^{18,19} For the parallel polarization configuration, the lowest signals in the FH images appear inside the area of scatterers, where the incident field is scattered into other polarizations, as opposed to the cross-polarized configurations, where the only nonzero signals appear inside the scattering area. One conspicuous detail about the FH images is that the reversed cross-polarized configurations, i.e., (x,y) - and (y,x) configurations, result in exactly the same images [cf. Figs. 6(b) and 6(c)]. However this is not the case for the SH images that are also much more sensitive to both light wavelength and polarization than the FH images. Such a striking difference is related to the circumstance that the reversed FH images correspond to the reciprocal SOM configurations that should produce the same images,³⁴ whereas the SH images are produced in the process of non-linear imaging so that the reversed configurations are not reciprocal. It is also seen that the SH images are considerably more sensitive to the wavelength than the FH images. We have previously suggested that very bright spots in the SH images occur due to the spatial overlap of properly polarized FH and SH eigenmodes,¹⁸ a conjecture that has also been indirectly confirmed with theoretical simulations.²⁰ The bright spots in SH images are therefore related to the positions of FH and SH eigenmodes both being sensitive to the wavelength. Consequently, the SH bright spots turn out to be much more sensitive to the wavelength than the FH bright

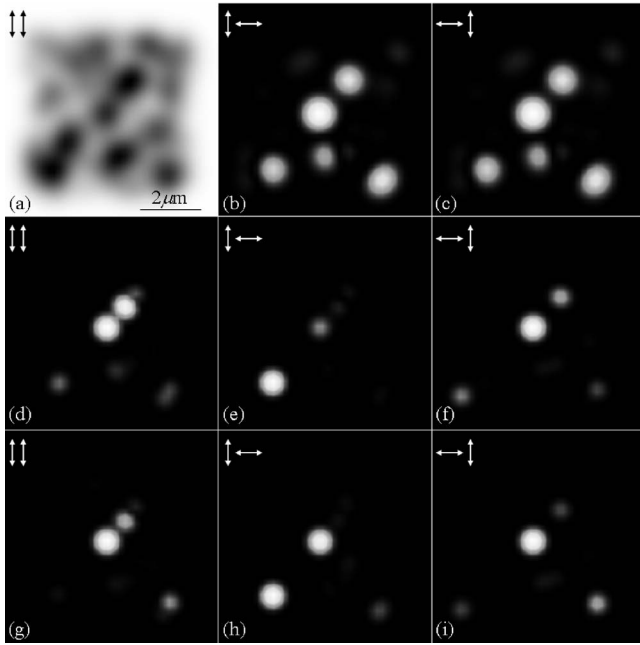


FIG. 8. Gray-scale (a)–(c) FH and (d)–(i) SH images ($7 \times 7 \mu\text{m}^2$) of the low-density sample simulated for the wavelength of (d)–(f) 750 and (g)–(i) 800 nm and the polarization configurations indicated by arrows (excitation, left arrow; detection, right arrow). The FH images at 800 nm (not shown) are found nearly identical to those at 750 nm. The maximum signals are 9700, 0.9, and 0.9 for FH images, 10×10^{-5} , 70×10^{-5} , and 25×10^{-5} for SH images obtained at 750 nm and 6×10^{-5} , 5.3×10^{-5} , and 14×10^{-5} for SH images obtained at 800 nm.

spots. Similar images were also calculated with the low-density sample. We observed that the wavelength and polarization sensitivity was, in this case, pronounced only for the SH images (Fig. 8). This very weak sensitivity of FH images to the wavelength can be explained by the fact that the low-density area mainly supports the weak interaction involving only a few individual scatterers that results in weak and broad resonances. Note that the corresponding FH signals in the cross-polarized configurations are one order of magnitude smaller than those for the high-density sample. Weaker depolarization indicates also weaker multiple scattering.

The SH images are, of course, also affected by the density of scatterers, exhibiting less sensitivity to both polarization and wavelength and featuring SH signals that are two orders of magnitude weaker than those for the high-density sample. Note that depolarization is essential for SHG in this configuration (Sec. IV C) and therefore its influence is more pronounced in the case of SH images than for the FH images. The observed decrease in SH signals is actually in good agreement with the decrease in the average SH signals measured in the experiments for the high- and low-density (50 and $25 \mu\text{m}^{-2}$, respectively) samples.¹⁹

C. Spatial overlap of FH and SH eigenmodes

In this section, we verify directly our conjecture that the most bright spots in the SH images occur due to spatial overlap of properly polarized FH and SH eigenmodes.¹⁸

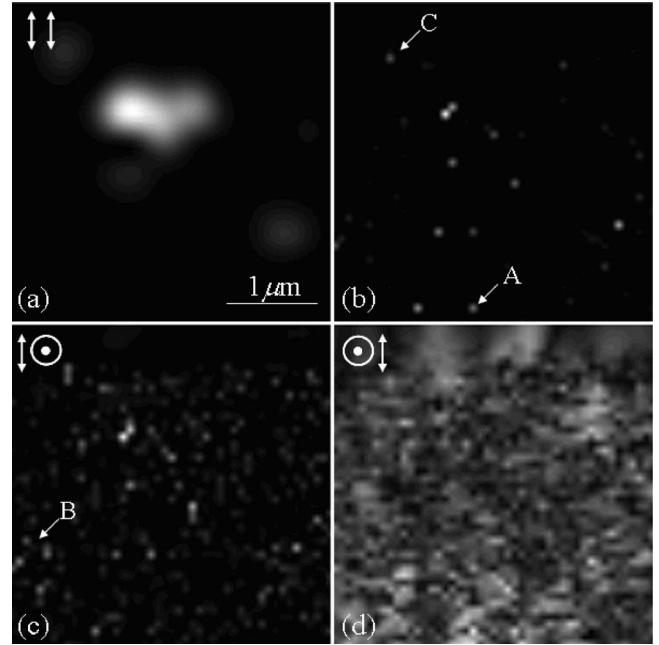


FIG. 9. Gray-scale zoom on a ($3.3 \times 3.3 \mu\text{m}^2$) simulated (a) SH image, (b) $[|E_{yz}(\omega, \mathbf{r})|^2 |E_{zy}(2\omega, \mathbf{r})|^2]$, (c) $|E_{yz}(\omega, \mathbf{r})|^2$, and (d) $|E_{zy}(2\omega, \mathbf{r})|^2$.

Here one should recall that we consider SHG as a process of generating a z component of the SH field by a z component of the FH field [Eq. (20)]. For instance, in order to investigate the bright SH spot in Fig. 6(d), which is obtained for y -polarized excitation and detection, one approach is to compare the squared z components $|E_{yz}(\omega, \mathbf{r})|^2$ of the FH fields (obtained for y -polarized uniform excitation [Fig. 4(f)]) with the y components $|E_{zy}(2\omega, \mathbf{r})|^2$ of a SH field distribution from the same area (obtained for z -polarized uniform excitation). Such a comparison could be performed by considering the distribution of the following product: $[|E_{yz}(\omega, \mathbf{r})|^2 |E_{zy}(2\omega, \mathbf{r})|^2]$. Figure 9 shows a zoom to the bright SH spot in Fig. 6(d) together with the corresponding distributions of the FH and SH fields and the above product.

As seen in Fig. 9 the brightest SH spot coincides with the strongest product peak. Furthermore, the remaining SH spots are also seen coinciding with the corresponding peaks in this product. Note that some peaks in the product can easily be recognized in the FH distribution $|E_{yz}(\omega, \mathbf{r})|^2$, but, for instance, the product peak at position A is not clearly seen at the corresponding position in this distribution. However, the SH distribution $|E_{zy}(2\omega, \mathbf{r})|^2$ has a strong spot at this location. In addition some spots in the FH distribution do not appear to produce peaks in the product (e.g., spots at B) or they appear changed (e.g., spot at C). It is also interesting that the maximum of the SH distribution (obtained at uniform excitation) is actually not coinciding with the strongest SH bright spot. One should bear in mind that the eigenmodes excited with an uniform illumination might be different from those excited by a tightly focused beam.

All in all these observations support the previously suggested explanation that the SH bright spots occur due to a spatial overlap of FH and SH eigenmodes, in the sense that

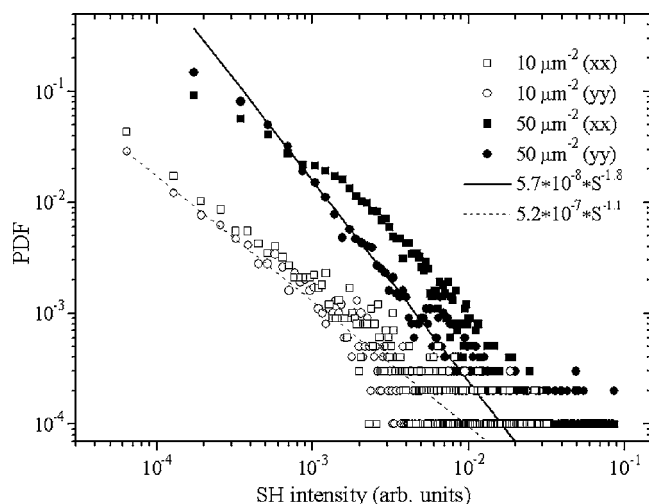


FIG. 10. PDFs based on the simulated SH images obtained in the parallel polarization configurations at 750 nm excitation wavelengths for both low and high density of scatterers. The PDF was made by dividing the difference between the maximum and minimum SH signal from each data set into 500 intervals and counting the number of points having signals within each of these intervals. The straight lines are fitted to the data for the (yy)-polarization configuration.

both the FH and SH simulated field distributions should be sufficiently enhanced at the locations of the SH bright spots.

D. Statistics of SH images

Another line of comparison of our modeling and experiments¹⁹ is related to the statistics of the SH enhancement in the corresponding images. In the experiments, a probability density function (PDF) was calculated for the spatial distribution of SH intensities in the low- and high-density areas. The PDF describes the probability of finding a given SH intensity (within some interval) in the considered area. It can be approximately determined from the experimental data by counting the number of intensity values falling within certain intensity intervals.^{35,36} For these simulations the number of points used to form the images was set to 100×100 and the difference between the minimum and maximum SH intensity was divided into 500 intervals. Figure 10 shows the resulting PDFs for the low- and high-density samples obtained from the SH images for 750 nm excitation wavelength and parallel polarization configurations [(xx) and (yy)].

As seen from Fig. 10 the low- and high-density configurations have different PDFs, while there is no apparent polarization dependence (as expected). For the high-density area the PDF is slightly shifted to higher SH intensities compared to the low-density area in accordance with the observed difference in SH intensities. The slopes of the line fits are ~ 1.8 and 1.1 for the high- and low-density area, respectively. These values are both lower than the value of 2.8 obtained in the experimental results. However, even though these values differ from the experiments it is important to note that the SH intensity actually does follow the power-law

dependence as expected with, for instance, fractal clusters of nanoparticles.³⁷ It is possible that the rather limited number of bright SH spots in the images compared to the experiments influence the statistics (especially for the low-density configuration). For instance, the flattening of the curve for high intensities could be related to the use of a limited data set, since part of the largest (but still widely different) SH intensities might be counted within each interval only once or twice, as seen by the pronounced splitup of the lowest PDF datapoints into clearly distinguishable horizontal lines. Furthermore, the difference between the use of a monochromatic incident field and radiation with a 15-nm-wide spectrum¹⁹ might be important for the statistics.

VI. CONCLUSION

In conclusion we have developed a model for the nonlinear microscopy of localized field enhancements in random metal nanostructures with a tightly focused laser beam scanning over a sample surface. We have used the analytic representations of the Green dyadic in the near- and far-field regions, with the latter being approximated by the part describing the scattering via excitation of surface plasmon polaritons. Two expressions for the involved Green dyadic, valid either for shorter or longer interaction distances, and a suitable limit to distinguish between the use of these expressions, were presented. Thus, composed Green dyadic represents an improvement of previous SPP simulations for periodic nanoparticles²³ and permits simulations for relatively close nanoparticles. Two sets of suitable nanoparticle coordinates, corresponding to the high and low density of scatterers, were generated and used for calculations of the self-consistent field distributions and the corresponding FH and SH images. The SH images for the high-density sample showed several bright spots, similar to those obtained in the experiments.^{18,19} The low-density images showed fewer similarities with these, however the observed large decrease in average SH signals is in good agreement with the experiments.¹⁹ Comparing FH and SH field distributions supported the idea of spatially overlapping FH and SH eigenmodes leading to bright spots in the SH-SOM images.^{18,19} All in all the simulation offers qualitative good agreement with the experimental results. We believe the developed approach can be used for simulating SH-SOM of metal nanoparticles (e.g., periodic arrays of nanoparticles) placed on metal surfaces with the SPP contribution to multiple scattering being taken into account. One can further apply this model to identify the most promising configurations of metal nanoparticles for achieving highly localized and enhanced fields. The nanoscale-localized high-intensity fields can be exploited in various prospective applications in nanoscience and nanotechnology, in particular, for optical probing of individual molecules and nanomodification.

ACKNOWLEDGMENTS

The authors acknowledge support from the European Network of Excellence, Plasmo-Nano-Devices (FP6-2002-IST-1-507879) and CONACyT Project number: 45999 (2004).

*Electronic address: jonas@physics.aau.dk

- ¹S. I. Bozhevolnyi, in *Optics of Nanostructured Materials*, edited by V. M. Markel and T. F. George (John Wiley & Sons, New York, 2001).
- ²*Optical Properties of Nanostructured Random Media*, edited by V. M. Shalaev (Springer-Verlag, Berlin, 2002).
- ³G. T. Boyd, T. Rasing, J. R. R. Leite, and Y. R. Shen, Phys. Rev. B **30**, 519 (1984).
- ⁴A. K. Sarychev and V. M. Shalaev, Phys. Rep. **335**, 275 (2000).
- ⁵M. Stockman, in *Optics of Nanostructured Materials*, edited by V. M. Markel and T. F. George (John Wiley & Sons, New York, 2001).
- ⁶H. R. Stuart and D. G. Hall, Phys. Rev. Lett. **80**, 5663 (1998).
- ⁷D. P. Tsai, J. Kovacs, Z. Wang, M. Moskovits, V. M. Shalaev, J. S. Suh, and R. Botet, Phys. Rev. Lett. **72**, 4149 (1994).
- ⁸S. I. Bozhevolnyi, I. I. Smolyaninov, and A. V. Zayats, Phys. Rev. B **51**, 17916 (1995).
- ⁹P. Zhang, T. L. Haslett, C. Douketis, and M. Moskovits, Phys. Rev. B **57**, 15513 (1998).
- ¹⁰S. I. Bozhevolnyi and V. Coello, Phys. Rev. B **58**, 10899 (1998).
- ¹¹V. A. Markel, V. M. Shalaev, P. Zhang, W. Huynh, L. Tay, T. L. Haslett, and M. Moskovits, Phys. Rev. B **59**, 10903 (1999).
- ¹²S. Grésillon, L. Aigouy, A. C. Boccara, J. C. Rivoal, X. Quelin, C. Desmarest, P. Gadenne, V. A. Shubin, A. K. Sarychev, and V. M. Shalaev, Phys. Rev. Lett. **82**, 4520 (1999).
- ¹³T. A. Leskova, A. A. Maradudin, and E. R. Méndez, in *Optical Properties of Nanostructured Random Media*, edited by V. M. Shalaev (Springer-Verlag, Berlin, 2002).
- ¹⁴I. Smolyaninov, A. Zayats, and C. C. Davis, Phys. Rev. B **56**, 9290 (1997).
- ¹⁵A. V. Zayats, T. Kalkbrenner, V. Sandoghdar, and J. Mlynek, Phys. Rev. B **61**, 4545 (2000).
- ¹⁶M. Breit, V. A. Podolskiy, S. Grésillon, G. von Plessen, J. Feldmann, J. C. Rivoal, P. Gadenne, A. K. Sarychev, and V. M. Shalaev, Phys. Rev. B **64**, 125106 (2001).
- ¹⁷C. Anceau, S. Brasselet, J. Zyss, and P. Gadenne, Opt. Lett. **28**, 713 (2003).
- ¹⁸S. I. Bozhevolnyi, J. Beermann, and V. Coello, Phys. Rev. Lett. **90**, 197403 (2003).
- ¹⁹J. Beermann and S. I. Bozhevolnyi, Phys. Rev. B **69**, 155429 (2004).
- ²⁰M. I. Stockman, D. J. Bergman, C. Anceau, S. Brasselet, and J. Zyss, Phys. Rev. Lett. **92**, 057402 (2004).
- ²¹S. I. Bozhevolnyi and V. Z. Lozovski, Phys. Rev. B **65**, 235420 (2002).
- ²²O. Keller, M. Xiao, and S. I. Bozhevolnyi, Surf. Sci. **280**, 217 (1993).
- ²³T. Søndergaard and S. I. Bozhevolnyi, Phys. Rev. B **67**, 165405 (2003).
- ²⁴A. B. Evlyukhin and S. I. Bozhevolnyi, Phys. Rev. B **71**, 134304 (2005).
- ²⁵Z. Li, B. Gu, and G. Yang, Phys. Rev. B **55**, 10883 (1997).
- ²⁶P. Gay-Balmaz and O. Martin, Opt. Commun. **184**, 37 (2000).
- ²⁷T. Søndergaard and S. I. Bozhevolnyi, Phys. Rev. B **69**, 045422 (2004).
- ²⁸E. D. Palik, *Handbook of Optical Constants of Solids* (Academic Press, New York, 1985).
- ²⁹J. E. Sansonetti and J. K. Furdyna, Phys. Rev. B **22**, 2866 (1980).
- ³⁰V. A. Markel, V. M. Shalaev, E. B. Stechel, W. Kim, and R. L. Armstrong, Phys. Rev. B **53**, 2425 (1996).
- ³¹B. T. Draine, Astrophys. J. **333**, 848 (1988).
- ³²E. M. Purcell and C. R. Pennypacker, Astrophys. J. **186**, 705 (1973).
- ³³R. W. Boyd, *Nonlinear Optics* (Academic Press, London, 1992).
- ³⁴E. R. Mendez, J.-J. Greffet, and R. Carminati, Opt. Commun. **142**, 7 (1997).
- ³⁵S. I. Bozhevolnyi and V. Coello, Phys. Rev. B **64**, 115414 (2001).
- ³⁶K. Seal, M. A. Nelson, Z. C. Ying, D. A. Genov, A. K. Sarychev, and V. M. Shalaev, Phys. Rev. B **67**, 035318 (2003).
- ³⁷M. I. Stockman, L. N. Pandey, L. S. Muratov, and T. F. George, Phys. Rev. Lett. **72**, 2486 (1994).